BIOCHEMISTRY
including biophysical chemistry & molecular biology

ARTICLE

pubs.acs.org/biochemistry

Murine Interleukin-3: Structure, Dynamics, and Conformational Heterogeneity in Solution

Shenggen Yao,[*,†,‡] Ian G. Young,[§] Raymond S. Norton,[†,∥] and James M. Murphy[*,†,‡]

[†]The Walter and Eliza Hall Institute of Medical Research, 1G Royal Parade, Parkville, Victoria 3052, Australia

[‡]Department of Medical Biology, The University of Melbourne, Parkville, Victoria 3010, Australia

[§]John Curtin School of Medical Research, Australian National University, Canberra, Australian Capital Territory 0200, Australia

[∥]Monash Institute of Pharmaceutical Sciences, Monash University, Parkville, Victoria 3052, Australia

Supporting Information

ABSTRACT: Interleukin-3 (IL-3), a cytokine produced primarily by activated T-cells during immune responses, is a crucial regulator of allergic inflammation. The three-dimensional structure of murine IL-3 (mIL-3) has remained elusive owing to its poor solubility and strong tendency toward aggregation under solution conditions typically used for structural studies. Here we describe the solution properties and structure of mIL-3 determined by NMR using an engineered construct of mIL-3 (mIL-3_{33-156}). mIL-3 adopts a four-helical bundle fold, typical of proteins belonging to the short-chain cytokine family, and features a core of highly conserved hydrophobic residues. While significant line broadening and peak disappearance were observed in NMR spectra at higher temperatures, there was no evidence for temperature-dependent changes of the oligomeric state of mIL-3_{33-156}. Further analysis of the temperature dependence of amide ^{1}H chemical shifts and backbone ^{15}N relaxation parameters, including ^{15}N relaxation dispersion, revealed the presence of significant conformational exchange and local conformational heterogeneity. Residues recently shown by mutagenesis to play key roles in β_{IL-3} receptor recognition and activation, which are located within the α_A and α_C helices and aligned on one face of the mIL-3_{33-156} structure, are relatively rigid. In contrast, pronounced conformational heterogeneity was observed for a cluster of residues located on the opposite side of mIL-3, which corresponds spatially to sites in the related cytokines human IL-3, IL-5, and GM-CSF that are known to mediate interactions with their respective α-receptor subunits. Such conformational heterogeneity may facilitate the interaction of mIL-3 with each of two naturally occurring mIL-3Rα isoforms, leading to structurally distinct high-affinity complexes.

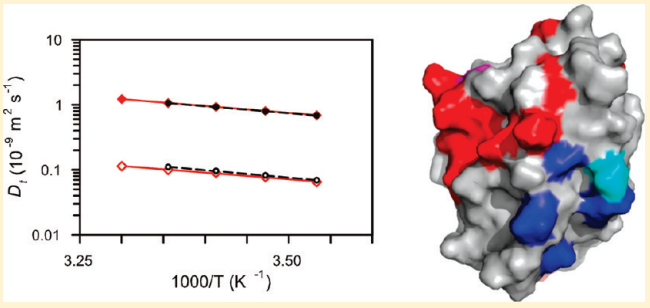

Interleukin-3 (IL-3), a cytokine produced primarily by activated T-cells during immune responses, promotes the proliferation and differentiation of myeloid progenitors.[1] IL-3 regulates the survival and proliferation of hematopoietic stem cells in the early stages of mouse embryonic development[2] and is critical for the induced basophil response and contributes to mast cell responses to parasite infections.[3] The importance of basophils in promoting T_H2 immune responses[4,5] also makes IL-3 an important regulator of allergic inflammation.

IL-3 exerts its biological effects upon target blood cells via binding to and subsequent activation of cell surface receptors composed of an IL-3-specific α-subunit and a β-subunit (βc) shared with the related cytokines granulocyte-macrophage colony-stimulating factor (GM-CSF) and interleukin-5 (IL-5). In mice, but not humans, an additional β-subunit, known as β_{IL-3}, which specifically binds mouse IL-3 (mIL-3), but not GM-CSF or IL-5, may also be utilized.[6] Binding of IL-3 to the extracellular portion of the IL-3 receptor leads to activation of the Janus kinases constitutively associated with the intracellular portions of the receptor subunits[7] by a poorly understood process, with subsequent induction of several signaling pathways.[8,9]

It has been shown recently that there are two IL-3Rα isoforms in mouse and human cells.[9] These isoforms influence the engagement between IL-3 and the β receptors and the signaling outcomes.[9] To understand the molecular basis of IL-3 receptor activation and signaling, it is essential to determine the three-dimensional structure of this cytokine. To date, the primary impediment to structural studies has been the unfavorable solution properties of recombinant mIL-3 expressed and purified from *Escherichia coli*, specifically its poor solubility, strong tendency to aggregate, and the heterogeneous disulfide bond pairing that arises during classical refolding.[10,11] Similar solution behavior was also observed for the wild-type human IL-3 (hIL-3) orthologue[12,13] and was overcome only by truncation of the N-terminal 14 and C-terminal 8 residues and the introduction of 14 amino acid substitutions to yield an analogue with improved solubility for which the solution structure could be determined.[13] By adopting a similar truncation strategy, we successfully

Received: November 11, 2010
Revised: February 15, 2011
Published: February 17, 2011

engineered a variant of mIL-3 with intrinsic high solubility, thus obviating the need for preparative refolding, while retaining biological activity comparable to full-length, wild-type mIL-3.[11] This engineered mIL-3 variant, mIL-3_{33-156}, comprises residues 33−156 of the proprotein encoded by the mIL-3 gene (SWISS-PROT accession number P01586) and contains a single amino acid substitution, C105A. Of the 32 N-terminal residues omitted in this mIL-3 variant, residues 1−26 encode a signal peptide that is cleaved upon secretion from IL-3 producing cells, while residues 27−32 (or 1−6 in mature mIL-3) are cleaved from mIL-3 produced by WEHI-3 cells, a common laboratory source of mIL-3.[14] Experimentally, we determined that the C-terminal residues 157−166 (corresponding to residues 131−140 in mature mIL-3) could be truncated to improve the solution properties of mIL-3 without compromising its bioactivity.[11] In addition, we eliminated the disulfide between Cys105-Cys166 (corresponding to Cys79-Cys140 in the mature form), a poorly conserved motif previously shown to be dispensable for mIL-3 activity.[10,11]

Collectively, these modifications to the mIL-3 expression construct have significantly improved both the yields from *E. coli* and the aqueous solubility of mIL-3_{33-156} sufficiently to permit structural studies to be performed. In this paper, we report its 3D structure and compare this structure with those of the related cytokines hIL-5,[15] hGM-CSF,[16] and the highly mutated human IL-3 analogue, SC-55494.[13] The structure reveals that residues within the α_A and α_C helices, recently shown to play key roles in $\beta_{IL\text{-}3}$ receptor recognition, are aligned on one face of mIL-3. Detailed investigations into the solution behavior, backbone dynamics, and conformational heterogeneity of mIL-3 identify a cluster of residues subject to significant conformational heterogeneity. The cluster of residues located on the side of the mIL-3_{33-156} four-helix bundle opposite to the β-receptor interaction interface corresponds spatially to sites in the related cytokines human IL-3, IL-5, and GM-CSF that are known to mediate the interaction with their respective α-receptor subunits. Conformational heterogeneity of these residues may underlie the capacity of mIL-3 to interact with each of the two naturally occurring mIL-3Rα isoforms, SP1 and SP2,[9,17] to enable the assembly of structurally distinct high-affinity signaling complexes.

EXPERIMENTAL PROCEDURES

Preparation of mIL-3_{33-156} Samples. The expression and purification of mIL-3_{33-156} used for the present studies have been described previously.[11,18] NMR samples were prepared by dissolving lyophilized ^{15}N-labeled (ca. 0.5, 1.0, or 2.0 mg) or ^{13}C/^{15}N-double-labeled (ca. 2.0 mg) mIL-3_{33-156} in 500 μL of H_2O containing 5% ^2H_2O, 20 mM potassium phosphate, and 0.02% (w/v) sodium azide at pH 6.7. A sample containing ca. 0.5 mg of ^{15}N-labeled mIL-3_{33-156} in 0.2 mM acetate, pH 4.3, was also prepared.

Translational Diffusion Measurements and Hydrodynamic Calculations. Translational self-diffusion coefficients of mIL-3_{33-156} and dioxane (as an internal reference of hydrodynamic radius),[19] at temperatures ranging from 283 to 303 K, were measured on a Bruker DRX600 spectrometer using a longitudinal eddy-current delay stimulated echo (LEDSTE) sequence incorporating a WATERGATE segment for water suppression, as described previously.[20,21] Diffusion coefficients, D_t, were then determined by fitting intensities of individual peaks in the aromatic and aliphatic regions to the following equation using the T_1/T_2 relaxation module in TOPSPIN (version 1.3, Bruker BioSpin):

$$I = I_0 \exp[-\gamma_H{}^2 g^2 \delta^2 (\Delta - \delta/3) D_t] \quad (1)$$

where γ_H is the gyromagnetic ratio of proton and g, δ, and Δ are the amplitude, duration, and separation of the single pair of gradient pulses, respectively. The hydrodynamic radius of mIL-3_{33-156} was estimated using the relationship $R_h = R_h{}^{REF}(D_t{}^{REF}/D_t)$, where $R_h{}^{REF}$ and $D_t{}^{REF}$ are the hydrodynamic radius and translational diffusion coefficient, respectively, of the reference molecule ($R_h{}^{REF}$ = 2.12 Å for dioxane).[19]

Chemical Shift Assignments and Structural Restraints. Chemical shift assignments of mIL-3_{33-156} have been deposited in BioMagResBank (http://www.bmrb.wisc.edu, with accession code 16614).[18] Distance restraints were derived from the intensities of NOE cross-peaks presented in ^{15}N-edited and ^{13}C-edited 3D NOESY-HSQC spectra (both with a mixing time of 120 ms) recorded using a Bruker Avance 800 spectrometer equipped with a cryoprobe. Backbone dihedral angle (ϕ and ψ) restraints were obtained from assigned chemical shifts using the program TALOS.[22] For the remaining residues, ϕ were restricted to negative values as the criteria for positive ϕ angle values were not met.[23]

Structure Calculations and Analysis. Initial structure calculations and optimization of experimental distance and angle restraints were performed using CYANA (version 2.1).[24] After the experimental restraints had been finalized, 200 structures were generated in XPLOR-NIH (version 2.17.0)[25] using torsion angle dynamics refinement and simulated annealing. Resultant structures were further refined in explicit water with energy minimization on the basis of experimental distance and angular restraints.[26] A family of 20 structures was then selected on the basis of stereochemistry and energy considerations and analyzed using PROCHECK-NMR[27] and MOLMOL.[28] Coordinates for the final set of 20 structures of mIL-3_{33-156} and associated structural restraints have been deposited in the Protein Data Bank[29] with accession code 2L3O.

Backbone Amide ^{1}H Temperature Coefficients. ^{1}H−^{15}N HSQC spectra of 0.15 mM mIL-3_{33-156} in 20 mM phosphate, pH 6.7, at 283, 288, 293, 298, and 303 K were recorded on a Bruker Avance500 spectrometer equipped with a cryoprobe. Temperature coefficients of backbone amide ^{1}H, excluding peaks heavily overlapped or displaying significant nonlinear temperature dependence, were determined by linear regression of amide ^{1}H chemical shifts versus temperature using SigmaPlot (version 8.0, Systat Software). Reported errors for temperature coefficients are standard deviations that resulted from the fitting. Temperature coefficients of mIL-3_{33-156} were classified into several groups based on their goodness of fits.

Backbone ^{15}N Relaxation Parameters, Rotational Diffusion Models, and Reduced Spectral Density Mapping. ^{15}N relaxation parameters, R_1, R_2, and steady-state ^{15}N−{^{1}H} NOE of mIL-3_{33-156} were measured using a sample containing 0.3 mM ^{15}N-labeled mIL-3_{33-156} in 20 mM potassium phosphate, pH 6.7, on a Bruker DRX600 at 283 and 298 K using pulse sequences similar to those available in Bruker pulse sequence library, as described previously.[30,31] Relaxation durations ranging from 10 ms to 1.5 s for R_1 and from 15.4 to 577.0 ms for R_2 were used. A complex data matrix of 2048 × 128 together with 32, 48, and 192 scans per t_1 increment were used for R_1, R_2, and steady-state ^{15}N−{^{1}H} NOE, respectively. The recycle times were 2.8 s for R_1 and R_2 and 3.8 s for the steady-state ^{15}N−{^{1}H} NOE,

respectively. All NMR spectra were processed using TOPSPIN (version 1.3 or 2.1, Bruker BioSpin) and analyzed with XEASY software (version 1.3).[32] ^{15}N relaxation rates R_1 and R_2 of backbone amides were obtained by fitting peak intensities at measured relaxation durations to a two-parameter single exponential decay using SigmaPlot (version 8.0, Systat Software). Reported errors for R_1 and R_2 were standard deviations resultant from nonlinear regression. The steady-state ^{15}N−{^{1}H} NOE values were calculated from peak intensity ratios obtained from spectra acquired in the presence and absence of proton saturation, with uncertainties estimated from background noise of the spectra.[33]

The program TENSOR2[34] was used for the evaluation of rotational diffusion models and estimation of isotropic rotational correlation time of mIL-3$_{33-156}$ using a group of backbone amides with steady-state ^{15}N−{^{1}H} NOE ≥ 0.65 and $|T_1/\langle T_1\rangle - T_2/\langle T_2\rangle| \leq 1.5$ SD[35] as well as a reduced group of residues with ^{15}N relaxation parameters satisfying the same conditions (NOE ≥ 0.65 and $|T_1/\langle T_1\rangle - T_2/\langle T_2\rangle| \leq 1.5$ SD) at both 283 and 298 K. Experimental fitting errors, χ_{exp}^2, resulting from isotropic, axially symmetric, and anisotropic rotational diffusion models were used to assess the significance of improvements for axially symmetric over isotropic and anisotropic over axially symmetric models, respectively, through the F_{test} values. $\chi_{0.05}^2$ values (referring to the $\alpha = 0.05$ confidence limit for the relevant fit derived from 500 Monte Carlo simulations[34]), as a convention adopted by the program TENSOR2, were used to assess whether a given diffusion model has converged (i.e., to be acceptable when $\chi_{exp}^2 < \chi_{0.05}^2$ or to be rejected when $\chi_{exp}^2 > \chi_{0.05}^2$). Although $\chi_{0.05}^2$ values suggested that none of the three models converged, the significant improvement revealed from statistical F_{test} for the anisotropic model over the axially symmetric and isotropic models led us to analyze ^{15}N relaxation data of R_1, R_2, and steady-state ^{15}N−{^{1}H} NOE using the program TENSOR2 with an anisotropic rotational diffusion model.

Reduced spectral density mapping analysis was also performed according to eqs 2−5:[36]

$$\sigma_{NH} = R_1(\text{NOE} - 1)\gamma_N/\gamma_H \quad (2)$$

$$J(0) = (6R_2 - 3R_1 - 2.72\sigma_{NH})/(3d^2 + 4c^2) \quad (3)$$

$$J(\omega_N) = (4R_1 - 5\sigma_{NH})/(3d^2 + 4c^2) \quad (4)$$

$$J(0.87\omega_H) = 4\sigma_{NH}/(5d^2) \quad (5)$$

where $d = (\mu_0 h\gamma_N\gamma_H/(8\pi^2))/\langle r^3_{NH}\rangle$, $c = \omega_N(\sigma_\parallel - \sigma_\perp)/3^{1/2}$, μ_0 is the permeability of free space, h is Planck's constant, γ_H and γ_N are the gyromagnetic ratio of ^{1}H and ^{15}N, respectively, r_{NH} is the average amide bond length (1.02 Å), and $(\sigma_\parallel - \sigma_\perp)$ is the chemical shift anisotropy for ^{15}N nuclei (=−170 ppm).

Backbone ^{15}N-Relaxation Dispersion Measurements. Backbone ^{15}N-relaxation dispersion measurements were performed by measuring in-phase and antiphase coherence-averaged ^{15}N transverse relaxation rates (R_2^{eff}) as a function of Carr−Purcell−Meiboom−Gill (CPMG) field strengths (ν_{CPMG} = 50, 80, 100, 120, 150, 200, 300, 400, 500, 600, 700, 800, and 1000 Hz) at 283 K and (ν_{CPMG} = 40, 80, 100, 120, 140, 160, 180, 200, 250, 300, 400, 500, 600, 700, 800, and 1000 Hz) at 298 K with a delay for the CPMG segment of T = 40 ms.[37,38] A recycle time of 2.5 s was used, and all other spectral parameters were similar to those used in the ^{15}N R_2 measurements described above. R_2^{eff} values were calculated from the ratio of peak intensity at a given CPMG field strength, $I(\nu_{CPMG})$, with the chosen duration of CPMG segment, T = 40 ms, and the corresponding peak intensity resulting from the same pulse sequence but with the CPMG relaxation segment omitted, I_0, via $R_2^{eff}(\nu_{CPMG}) = (-1/T)\ln[I(\nu_{CPMG})/I_0]$.[38] R_2^{eff} values of each residue were then fitted on a residue-by-residue basis with the fast-limit equation:[37,39]

$$R_2^{eff}(\nu_{CPMG}) = \varepsilon R_{in} + (1-\varepsilon)R_{anti} + R_{ex} = R_2^{ave} + (\omega_A - \omega_B)^2 p_A p_B \tau_{ex}[1 - 8\tau_{ex}\nu_{CPMG}\tanh(1/(8\nu_{CPMG}\tau_{ex}))] \quad (6)$$

where R_2^{ave} is the transverse relaxation rate averaged over the in-phase and antiphase coherence. ω_A, p_A, ω_B, and p_B are resonance frequencies and populations for nuclear spin in sites A and B, respectively, τ_{ex} is the time constant for the exchange process, and ν_{CPMG} is defined as $1/(4\tau_{CPMG})$, with $2\tau_{CPMG}$ being the separation between the center of two successive 180° pulses in the CPMG segment.

RESULTS

Solution Characteristics of mIL-3$_{33-156}$. The solution properties of mIL-3$_{33-156}$ were evaluated in acetate buffer (pH 4.3) and phosphate buffer (pH 6.7) between 283 and 303 K by monitoring ^{1}H−^{15}N HSQC spectra and comparing hydrodynamic radii calculated from translational diffusion coefficients measured by PFG-NMR. ^{1}H−^{15}N HSQC spectra of mIL-3$_{33-156}$ in phosphate, pH 6.7, from 283 to 303 K are shown in Figure 1A, and a comparison with spectra in acetate buffer, pH 4.3, at 283 and 298 K, is presented in Figure S1 (Supporting Information). Experimentally measured translational diffusion coefficients of mIL-3$_{33-156}$ and a reference molecule, dioxane, together with the subsequently calculated hydrodynamic radii of mIL-3$_{33-156}$ are tabulated in Table 1. Translational diffusion induced signal attenuation in the presence of pulsed-field gradients for both mIL-3$_{33-156}$ and dioxane are shown in Figure 1B,C, and the temperature dependence of translational diffusion coefficients in the form of Arrhenius plots is shown in Figure 1D. Three pairs of ^{1}H−^{15}N HSQC spectra for mIL-3$_{33-156}$ in 20 mM phosphate (pH 6.7) recorded at 283 and 298 K with concentrations of 0.22, 0.30, and 0.44 mM, respectively, are shown in Figure S2 (Supporting Information); significant deterioration in spectra quality was observed at >0.4 mM.

Solution Structure of mIL-3$_{33-156}$. The optimal solution conditions were established to be 20 mM potassium phosphate, pH 6.7, and 283 K. Under these conditions, near-complete assignments of ^{1}H, ^{15}N, and ^{13}C chemical shifts were obtained using standard triple-resonance heteronuclear experiments.[18] A total of 1209 nonredundant distance restraints obtained from ^{15}N- and ^{13}C-edited NOESY spectra, together with 180 dihedral angle restraints derived from secondary chemical shifts and 28 hydrogen bond restraints (all within individual helices), were used in calculating the 3D structure of mIL-3$_{33-156}$. The statistics for the 20 lowest energy structural models (Table 2) indicate that they fit well with experimentally derived distance and angle restraints. A summary of backbone angular order parameters of the mIL-3$_{33-156}$ ensemble is presented in Figure S3 (Supporting Information). Figure 2 shows the ensemble of the 20 lowest energy solution structures superimposed over the backbone heavy atoms (N, C$^\alpha$, and C′) of the four α-helices as well as

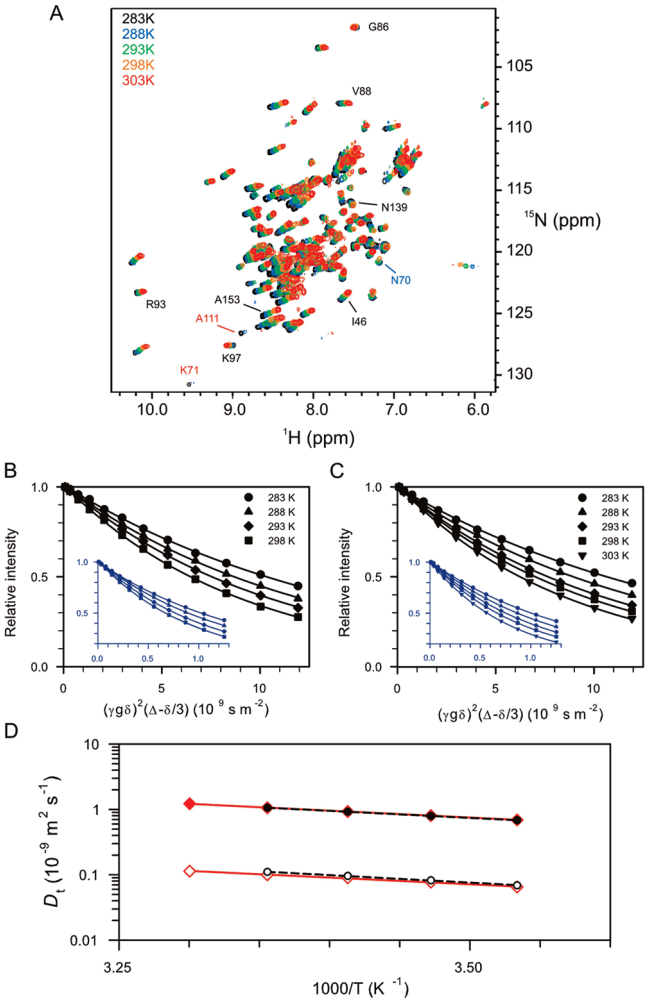

Figure 1. ^{1}H−^{15}N HSQC spectra of mIL-3$_{33-156}$ from 283 to 303 K and translational diffusion coefficients measured by PFG-NMR. (A) Overlay of ^{1}H−^{15}N HSQC spectra of mIL-3$_{33-156}$ in 20 mM phosphate, pH 6.7, recorded from 283 to 303 K. Peaks with temperature-dependent amide proton chemical shifts and linear regression shown in Figure 3A are labeled, and peaks that disappear at higher temperature are also indicated. Translational diffusion induced signal attenuations in the presence of pulsed-field gradients are shown as relative intensities versus the strength of diffusion encoding, $\gamma^2 g^2 \delta^2(\Delta - \delta/3)$, for mIL-3$_{33-156}$ in 20 mM phosphate, pH 6.7 (B), and in 0.2 mM acetate, pH 4.3 (C). Corresponding data for the internal reference of the hydrodynamic radius, dioxane, are shown in the insets of (B) and (C), respectively (diffusion measurement for mIL-3$_{33-156}$ in 20 mM phosphate at 303 K was not performed). All of the lines in (B) and (C) represent the results of nonlinear regression to eq 1. (D) Translational diffusion coefficients of mIL-3$_{33-156}$ (open symbols) and internal reference molecule, dioxane (filled symbols), versus 1000/T in 20 mM phosphate, pH 6.7 (black), and in 0.2 mM acetate, pH 4.3 (red). Both dashed and solid lines represent fits to the Arrhenius function for the temperature dependence of translational diffusion coefficients.

cartoons depicting the secondary structure of mIL-3, highlighting the hydrophobic residues packed in the core of the four-helical bundle structure and residues involved in β_{IL-3} receptor binding,[17] and a surface representation of mIL-3$_{33-156}$ with charged residues highlighted. mIL-3$_{33-156}$ adopts the four-helical bundle fold characteristic of all short-chain cytokines, consisting of helices α_A (residues Asn42−Leu54), α_B (Arg74−Glu87), α_C (Lys97−Cys106), and α_D (Leu124−His137). The structure also features a network of highly conserved hydrophobic residues packed in the core of the four-helical bundle structure, contributed by the α_A (Ile46, Val47, Ile50, Leu54), α_B (Leu78, Val82), α_C (Ile96, Leu100, Leu103), and α_D (Leu131, Met135) helices (Figure 2C).

Temperature Coefficients of Backbone Amide ^{1}H Chemical Shifts of mIL-3$_{33-156}$. Significant variations in peak intensity in the ^{1}H−^{15}N HSQC spectra of mIL-3$_{33-156}$, including the absence of peaks corresponding to several residues at 298 K and above (Figure 1A), imply the presence of local conformational heterogeneity.[40] An analysis of the temperature dependence of backbone amide ^{1}H chemical shifts of mIL-3$_{33-156}$ in phosphate buffer at pH 6.7 was therefore carried out. While most backbone amide ^{1}H chemical shifts displayed a linear dependence on temperature, a group of residues exhibited deviations from linearity at 298 K and above (Figure 3A). Temperature coefficients of backbone amide protons are summarized in Figure 3B. Residues with backbone amide ^{1}H chemical shifts that deviated significantly from linearity, including Asn42, Cys43, Lys60, Arg69, Ser72, Ser79, Glu83, Val95, Leu100, Asp126, Lys129, Leu138, Asp140, Leu141, Glu142 (goodness of linear regression less than 0.85; colored magenta) and Asn70, Lys71, Ala111 (peaks disappeared at temperature higher than 298 K; colored red), are highlighted on the surface diagram of mIL-3$_{33-156}$ in Figure 3C. While some of these residues are scattered around the molecule, a subgroup clustered together with Asn70, Lys71, and Ala111.

^{15}N Relaxation Parameters of mIL-3$_{33-156}$. To further investigate the internal dynamics of mIL-3$_{33-156}$, backbone ^{15}N relaxation parameters, R_1, R_2, and steady-state ^{15}N−{^{1}H} NOE, were measured at 283 and 298 K. These data are summarized in Figure 4 and tabulated in Table S1 (Supporting Information); representative R_1 and R_2 decay curves including nonlinear regression are also shown in Figure S4 (Supporting Information). After the exclusion of resonances either heavily overlapped or with weak peak intensities due to line broadening, R_1, R_2, and steady-state ^{15}N−{^{1}H} NOE values were obtained for a total of 112 backbone amides (there are 9 prolines in mIL-3$_{33-156}$) at 283 K. In contrast, owing to poor spectral quality of mIL-3$_{33-156}$ at higher temperature, R_1, R_2, and steady-state ^{15}N−{^{1}H} NOE values were obtained for only 91 backbone amides at 298 K (Figure 4). Average values of R_1, R_2, and steady-state ^{15}N−{^{1}H} NOE over those 91 backbone amides with relaxation data measured at both temperatures as well as average values over the helical regions and individual helices are summarized in Table 3. As expected, a decrease in R_1 and an increase in R_2 were found for mIL-3$_{33-156}$ at 283 K because it tumbles more slowly than at 298 K. ^{15}N−{^{1}H} NOE values increased at 283 K relative to 298 K, consistent with the backbone internal motion on the picosecond to nanosecond time scale being more restrained at 283 K.

Model-Free Analysis and Reduced Spectral Density Mapping. With a view to further understanding the internal dynamics within mIL-3$_{33-156}$, we analyzed the experimentally measured backbone ^{15}N relaxation parameters using model-free analysis and reduced spectral density mapping. From the closest to mean structure of mIL-3$_{33-156}$, the principal moments of its inertia tensor were calculated to be 1.000:0.803:0.511, indicating the apparent anisotropic nature of its global rotational reorientation. Relaxation parameters of a group of backbone amides (51 for 283 K and 37 for 298 K) satisfying both steady-state ^{15}N−{^{1}H} NOE ≥ 0.65 and $|T_1/\langle T_1\rangle - T_2/\langle T_2\rangle| \leq 1.5$ SD[35] were used for the evaluation of its rotational diffusion tensor using the program

Table 1. Translational Diffusion Coefficients of mIL-$3_{33\text{-}156}$ and Dioxane Measured by PFG-NMR and Calculated Hydrodynamic Radius for mIL-$3_{33\text{-}156}$

	20 mM phosphate, pH 6.7			0.2 mM acetate, pH 4.3		
T (K)	$D_t^{\text{mIL-3}}$ (10^{-11} m^2/s)	D_t^{dioxane} (10^{-10} m^2/s)	R_h (Å)[a]	$D_t^{\text{mIL-3}}$ (10^{-11} m^2/s)	D_t^{dioxane} (10^{-10} m^2/s)	R_h (Å)[a]
283	6.89 ± 0.12	6.82 ± 0.06	20.98	6.50 ± 0.02	6.89 ± 0.05	22.47
288	8.19 ± 0.13	7.91 ± 0.11	20.49	7.72 ± 0.02	8.05 ± 0.04	22.11
293	9.58 ± 0.31	9.21 ± 0.11	20.37	8.98 ± 0.09	9.29 ± 0.04	21.93
298	11.04 ± 0.18	10.58 ± 0.07	20.31	9.97 ± 0.06	10.59 ± 0.03	22.51
303				11.34 ± 0.13	12.22 ± 0.10	22.85

[a] $R_h = R_h^{\text{dioxane}}(D_t^{\text{dioxane}}/D_t^{\text{mIL-3}})$ with R_h^{dioxane} = 2.12 Å.[19]

TENSOR2.[34] From these two groups of residues, a reduced group of 26 residues (of these 26 residues, 22 residues are from the four main helices) which satisfy the same conditions at both 283 and 298 K were also tested from rotational diffusion models. All of the fitting results together with statistical test outcomes are summarized in Table 4. As can be seen from Table 4, for all of the diffusion models tested with either the original group of residues (51 residues for 283 K and 37 for 298 K) or the reduced group of residues (26 residues), all χ_{exp}^2 values are larger than $\chi_{0.05}^2$ values (refers to the $\alpha = 0.05$ confidence limit for the relevant fit derived from 500 Monte Carlo simulations).[34] Based on the convention used by the program TENSOR2, this ($\chi_{exp}^2 > \chi_{0.05}^2$) would suggest that none of these diffusion tensor models had converged. The experimentally measured ^{15}N relaxation parameters of mIL-3_{33-156} may have failed the test of Monte Carlo simulations in the optimization of rotational diffusion tensor owing to the presence of poorly defined regions near the N- and C-terminal and local conformational heterogeneity. On the other hand, statistical F_{test} values among the models indicate that the axially symmetric model is a significant improvement over the isotropic model at both 283 and 298 K and the anisotropic model is significant improvement over the axially symmetric model at 283 K. It is also clear that the anisotropy of the rotational diffusion tensor derived from the reduced group of 26 residues at 283 and 298 K agrees better than that obtained from the original group of residues (Table 4).

Model-free analysis results obtained using rotational diffusion tensor parameters derived from that reduced set of 26 residues are presented here and are summarized in Figure 5 and tabulated in Table S2 (Supporting Information). One hundred three residues out of 112 with ^{15}N relaxation parameters measured at 283 K were fitted successfully to one of five combinations of model-free parameters (22 residues for model 1 (S^2), 29 for model 2 (S^2 and τ_e), 12 for model 3 (S^2 and R_{ex}), 28 for model 4 (S^2, τ_e, and R_{ex}), and 12 for model 5 (S_s^2, S_f^2, and τ_e)), whereas 86 residues out of 91 with ^{15}N relaxation parameters measured at 298 K were fitted successfully to one of five combinations of model-free parameters (18 residues for model 1 (S^2), 28 for model 2 (S^2 and τ_e), 5 for model 3 (S^2 and R_{ex}), 29 for model 4 (S^2, τ_e, and R_{ex}), and 6 for model 5 (S_s^2, S_f^2, and τ_e)). Average S^2 values for the four α-helices are 0.86 ± 0.12 and 0.85 ± 0.15 at 283 and 298 K, respectively (calculated from a total of 32 residues fitted successfully at both 283 and 298 K). Average S^2 values for individual helices are as follows: helix A (9 residues), 0.88 ± 0.14 and 0.89 ± 0.14 for 283 and 298 K, respectively; helix B (7 residues), 0.91 ± 0.11 and 0.86 ± 0.08; helix C (7 residues), 0.84 ± 0.13 and 0.72 ± 0.22; and helix D (9 residues), 0.81 ± 0.11 and 0.92 ± 0.08. It should be noted that lower S^2 values would have been expected at the higher temperature, although it is possible that the apparent higher S^2 value for helix D at 298 K compared with that at 283 K in particular may have been caused by the different combinations of model-free parameters fitted at 283 and 298 K in the present study (Table S2, Supporting Information).

Given the presence of poorly defined N- and C-termini and local conformational heterogeneity, which we believe to be responsible for the less than satisfactory determination of its rotational diffusion tensor as described above, we have also calculated reduced spectral density functions for ^{15}N relaxation parameters of mIL-3_{33-156} (eqs 2−5), which make no assumptions about the nature of molecular global rotational diffusion;[36] the resulting

Table 2. Summary of Restraints Used in the Structure Calculation and Structural Statistics for the 20 Final Structures of mIL-$3_{33\text{-}156}$

distance restraints	1209
intra ($i = j$)	388
sequential ($\|i - j\| = 1$)	376
short ($1 < \|i - j\| \leq 5$)	203
long ($\|i - j\| > 5$)	242
dihedral restraints	180
hydrogen bonds	28
deviations from experimental data	
NOEs (Å)	0.0364 ± 0.0024
dihedrals (deg)	0.76 ± 0.10
deviations from ideal geometry	
bonds (Å)	0.0060 ± 0.0001
angles (deg)	0.711 ± 0.017
impropers (deg)	0.528 ± 0.013

rms deviations (Å)	N, C^α, C′	all heavy atoms
helices [a]	0.68 ± 0.10	1.66 ± 0.22
residues 43−136	1.16 ± 0.18	2.09 ± 0.24

Ramachandran plot[b]	helical regions	overall
most favored regions (%)	99.5	72.4
additionally allowed regions (%)	0.1	21.7
generously allowed regions (%)	0.4	5.0
disallowed (%)	0.0	0.9

[a] Mean pairwise rmsd (root-mean-square deviation) over four helices (residues 43−53, 74−85, 96−106, and 124−136). [b] As determined by program PROCHECK_NMR for residues of mIL-3_{33-156} except Gly and Pro.

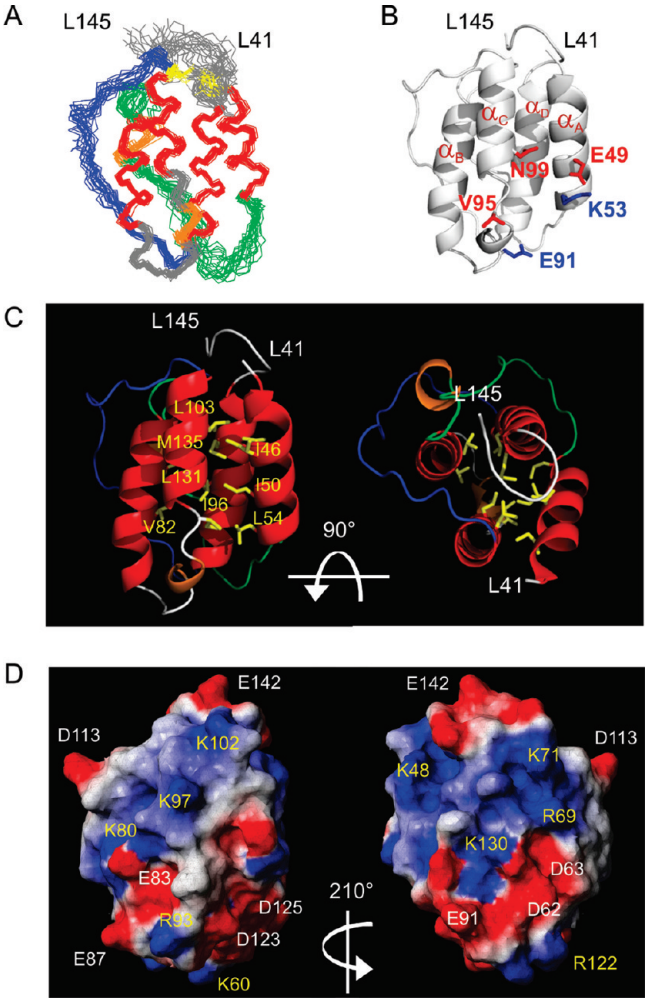

Figure 2. Solution structure of mIL-3. (A) Backbone of the final 20 solution structures superimposed over backbone heavy atoms (N, C^{α}, and C′) of four α-helices (42−53, 74−85, 96−106, and 124−136). Color scheme: red, four α-helices; green, α_A-α_B loop; gray, α_B-α_C loop; blue, α_C-α_D loop. Two single-turn 3_{10} helices (residues 67−69 and 92−94), which were observed in only a fraction of the final 20 structures within the α_A-α_B and α_B-α_C loops, are highlighted in orange, and the disulfide bond between Cys43 and Cys106 is shown in yellow. (B) Structure of mIL-3, in the same orientation as in (A), with side chains of residues important for $\beta_{IL\text{-}3}$ receptor binding highlighted. Residues drawn as red and blue sticks are crucial for mIL-3 binding to $\beta_{IL\text{-}3}$ in the absence or presence of the mIL-3Rα SP2 isoform, while a subset of these residues, Lys53 and Glu91 (blue sticks), plays a vital role in mIL-3 binding and activation of $\beta_{IL\text{-}3}$ in the presence of the mIL-3Rα SP1 subunit.[17] (C) Structure of mIL-3, left cartoon in the same orientation as in (A), with side chains of hydrophobic core residues shown in yellow sticks. (D) Surface representation of mIL-3, left side figure in the same orientation as in (A), showing basic residues in blue and acidic residues in red. (A) and (D) were created using MOLMOL[28] and (B) and (C) using PyMOL (DeLano, 2004; http://pymol.sourceforge.net).

values are summarized in Figure 6. Attempts to estimate approximate order parameters from $J(0)$ and $J(\omega_N)$[41,42] also failed as this analysis resulted in a large proportion of residues with S^2 values >1, further suggesting the presence of significant R_{ex} contributions to the experimentally measured R_2 values, as noted previously.[43] This observation is consistent with the large number of backbone amides requiring the presence of an R_{ex} term to obtain satisfactory fits in model-free analysis (see Discussion).

Local Conformational Exchange Measured by ^{15}N Transverse Relaxation Dispersion. The observed nonlinear temperature dependence of protein backbone amide ^{1}H chemical shifts strongly implies the presence of local conformational heterogeneity, which may originate from a variety of sources, including access to alternative low free-energy excited states of folded proteins by local residues.[44] Therefore, we performed measurements of ^{15}N transverse relaxation dispersions at 283 and 298 K, aiming to detect experimentally any residues that occupy low populated excited states.[45,46] While there are fluctuations in terms of R_2^{eff} values against CPMG field strength, ν_{CPMG}, at 283 K, a lack of consistent changes of R_2^{eff} values indicates the absence of significant conformational exchange on the submillisecond to millisecond time scales. In contrast, conformational exchange on the submillisecond to millisecond time scale is clearly evident at 298 K, with the following 23 residues showing significant conformational exchange as detected by CPMG relaxation dispersions: Glu49, Lys60, Leu68, Asn70, Arg74, Val76, Ser79, Lys80, Gln101, Lys102, Cys106, Leu107, Asn112, Asp113, Ser114, Ala115, Val119, Met135, His137, Leu138, Asp140, Thr143, and Leu145 (Table S5, Supporting Information). Cross-peaks of Lys71 and Ala111 were not observed at 298 K in the ^{1}H−^{15}N HSQC spectrum and were thus not amenable to ^{15}N relaxation dispersion measurement. Representative ^{15}N relaxation dispersion curves for mIL-3_{33-156} at 283 and 298 K and the difference in effective transverse relaxation rates at two ν_{CPMG} fields are shown in Figure 7A−C. Figure 7D shows a surface representation of mIL-3_{33-156}, where backbone amides of residues that access alternative conformations on the submillisecond to millisecond time scales, as detected by ^{15}N relaxation dispersion, and those important for its binding to $\beta_{IL\text{-}3}$ are highlighted. For comparison, the residues in human IL-3 (Figure 7E) and human GM-CSF (Figure 7F) defined by mutagenesis[47] and X-ray crystallography,[48] respectively, to mediate interaction with their cognate α-receptors are highlighted in their corresponding surface representations. Additionally, homology modeling and mutagenesis have indicated that the surface of human GM-CSF that mediates α-receptor binding will be larger than that revealed by the complex crystal structure, as no electron density was observed for the GM-CSFRα N-terminal Ig-like domain: a domain since shown to play an important role in GM-CSF binding.[49]

DISCUSSION

Although mIL-3 conveys essential biological signals in blood cell development and inflammatory responses, structural studies of this important protein have been confounded by its intrinsic poor solubility and strong tendency to aggregate in solution. A recently developed soluble variant of mIL-3, mIL-3_{33-156}, which retains wild-type biological activity and exhibits significantly improved solution behavior,[11] has enabled us to perform a comprehensive characterization of its 3D solution structure, backbone dynamics, and hydrodynamic properties in two different buffer solutions over the temperature range 283−303 K. We begin by comparing the structure of mIL-3_{33-156} with structures of the hIL-3 analogue SC-55494, GM-CSF, and IL-5 and then evaluate the novel features of mIL-3_{33-156} revealed in the current study.

Comparison of the Solution Structure of mIL-3_{33-156} with the Solution Structure of the hIL-3 Analogue and Crystal Structures of Human GM-CSF and IL-5. mIL-3 adopts the four-helical bundle fold, typical of proteins belonging to the short-chain cytokine family, where α_A and α_C pack side-by-side

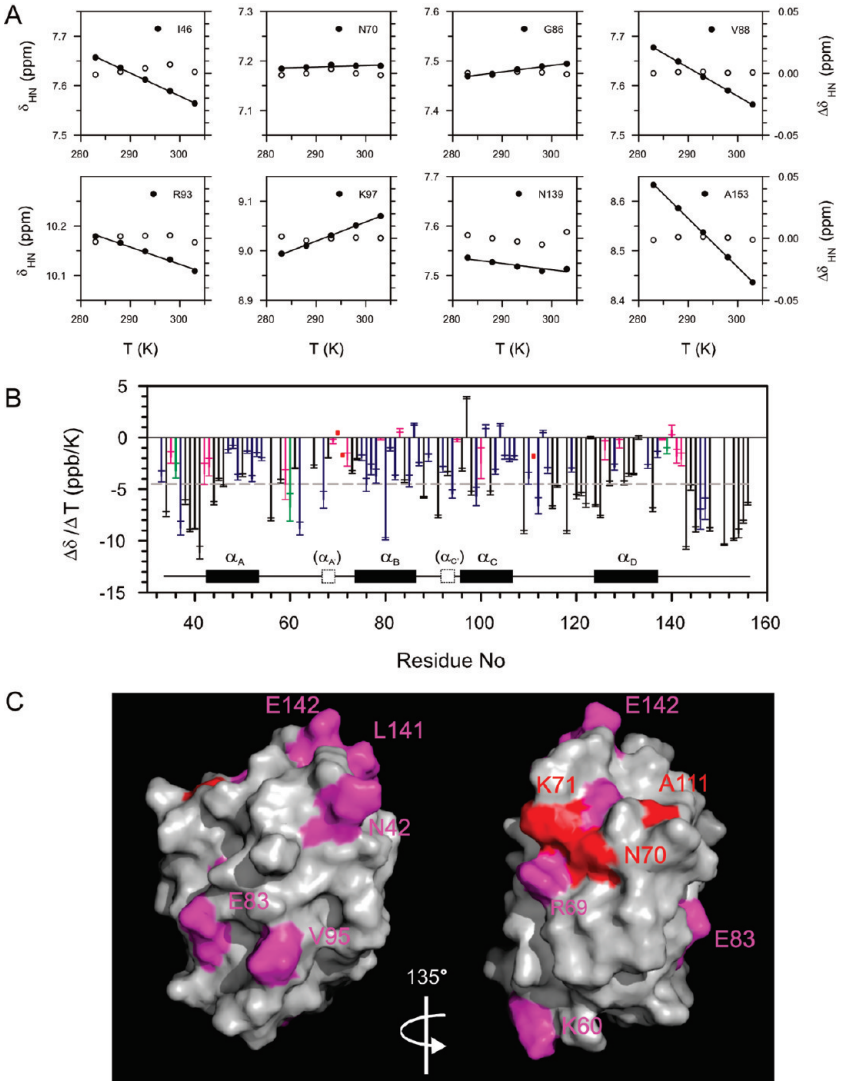

Figure 3. Temperature dependence of mIL-3_{33-156} in 20 mM phosphate, pH 6.7. (A) Plots of backbone amide ^{1}H chemical shifts of mIL-3_{33-156} (left *Y*-axis, filled symbols) and residual chemical shifts after the subtraction of fitted values (right *Y*-axis, unfilled symbols) versus temperature. Lines represent linear regression of chemical shifts against temperature. (B) Temperature coefficients for backbone amides of mIL-3_{33-156} versus sequence number, color coded using the goodness of fit of linear regression as follows: $R^2 > 0.99$ (black bar), $0.9 < R^2 \leq 0.99$ (blue bar), $0.85 < R^2 \leq 0.9$ (green bar), and $R^2 \leq 0.85$ (pink bar). Residues Asn70, Lys71, and Ala111, with their temperature coefficients not determined due to corresponding peaks significantly weakened/disappeared at higher temperature, are indicated with red squares. Also shown in (B) is a schematic of secondary structural elements of mIL-3_{33-156} as revealed from its solution structure. (C) Surface diagrams, left side figure is drawn in the same orientation as Figure 2A, showing residues with significant nonlinear temperature dependence (goodness of fit of linear regression less than 0.85) or peaks that disappear at temperature 298 K and above. The surface diagram (C) was created using the program PyMOL (DeLano, 2004; http://pymol.sourceforge.net).

and antiparallel to one another, tethered by the disulfide bond between Cys[43] in α_A and Cys[106] in α_C, with the α_D and α_B helices packing behind the α_A and α_C helices, respectively, in an antiparallel fashion (Figure 2). Although not adjacent, the α_A and α_B helices are parallel to one another, and the α_C and α_D are similarly parallel to one another, leading to this topology being referred to as an "up−up−down−down" fold.[50] There is remarkable conservation in the topology of the four-helical bundles adopted by mIL-3_{33-156}, the hIL-3 analogue (SC-55494), hGM-CSF, and hIL-5 (Figure S5A, Supporting Information). Pairwise superimposition of the backbone atoms of the four helices of mIL-3_{33-156} (42−53, 74−85, 96−106, and 124−136) with the corresponding atoms in hIL-3 (34−45, 73−84, 93−103, and 123−135), hGM-CSF (31−42, 72−83, 100−110, and 120−132), and hIL-5 (25−36, 64−75, and 87−97 of A-chain and 112−1124 of B-chain) yielded root-mean-square deviations (rmsd) of 2.22, 2.31, and 2.65 Å, respectively. This compares to an rmsd between backbone heavy atoms in helical regions (residues 42−53, 74−85, 96−106, and 124−136) among the 20 lowest energy structural models of mIL-3_{33-156} of 1.25 Å. Despite the remarkable convergence of their four-helical bundle folds, there is very low amino acid sequence identity among mIL-3, hIL-3, hGM-CSF, and hIL-5, with only five identical residues and 16 conservative substitutions (Figure S5B, Supporting Information). Strikingly, 18 of these 21 residues have hydrophobic side chains, and inspection of the mIL-3, hIL-3, hGM-CSF, and hIL-5 structures shows that these residues mediate the conserved hydrophobic contacts that stabilize the four-helical bundle topology (Figure 2C).

The four-helical bundle fold relies on the long interhelical loops that connect α_A to α_B and α_C to α_D, which are highly

variable in sequence and length between mIL-3 and hIL-3, as well as the other family members hGM-CSF and hIL-5 (Figure S5, Supporting Information). In fact, hIL-5 exists as a homodimer in nature owing to the relatively short α_C-α_D loop, which prevents a hIL-5 monomer from adopting the up−up−down−down fold and thus favors domain swapping of α_D between protomers.[51] The divergent interhelical loop sequences and lengths have hampered the generation of structural models for mIL-3 based on the solution structure of the hIL-3 analogue (SC-55494),[13] a mIL-3 relative with only 29% sequence identity. For example, the mIL-3 α_A-α_B loop is seven residues shorter than the corresponding region in the hIL-3 sequence and contains a helix-breaking proline residue in the region corresponding to the hIL-3 α_A' helix (Figure S5, Supporting Information). The structure of mIL-3_{33-156} presented herein has resolved this conundrum by determining that, in contrast to the hIL-3 analogue, the mIL-3 α_A' helix consists of only a single helical turn. In addition, like the hGM-CSF structure but in contrast to that of the hIL-3 analogue, a helical turn was observed in the mIL-3 α_B-α_C loop (Figure S5A, Supporting Information). In contrast to the structures of hGM-CSF and hIL-5, however, neither mIL-3_{33-156} nor the hIL-3 analogue possesses any β-strand elements in their α_A-α_B and α_C-α_D loops (Figure S5A, Supporting Information).

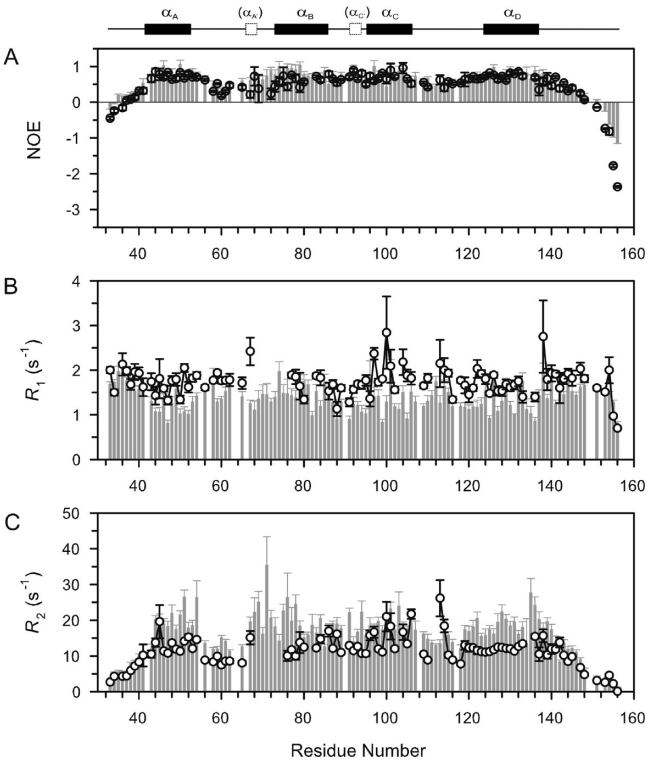

Figure 4. Backbone ^{15}N relaxation parameters of mIL-3_{33-156} measured at ^{15}N frequency of 60.81 MHz. (A) Steady-state ^{15}N−{^{1}H} NOE, (B) R_1, and (C) R_2 at 283 K (gray bars) and 298 K (open circles). A schematic showing secondary structural elements of mIL-3_{33-156} is shown at the top. Representative R_1 and R_2 decay curves including nonlinear regression for a group of selected residues are shown in Figure S4 (Supporting Information).

Solution Characteristics of mIL-3_{33-156}. One of the common causes of poor solution behavior is aggregation/oligomerization of the protein. An increase in apparent molecular mass generally results in a slower overall tumbling, giving rise to peaks with broad line widths in NMR spectra. The hydrodynamic radius as estimated from experimentally measured translational diffusion coefficients in two different buffer conditions (acetate at pH 4.3 and phosphate at pH 6.7), however, gave no evidence for changes in the oligomeric state of mIL-3_{33-156} over the temperature range 283−303 K. As can be seen from Table 1 and Figure 1C, translational diffusion coefficients of mIL-3_{33-156} versus temperature in both solutions are well described by the Arrhenius function, indicating that the translational diffusive behavior of mIL-3_{33-156} is consistent overall with the Stokes−Einstein model between 283 and 303 K. Although the structural study of the hIL-3 analogue SC-55494 was performed at pH 4.6 and 300 K,[12,13] we found mIL-3_{33-156} gave consistently poor spectral dispersion and broader line widths relative to the corresponding spectra obtained in 20 mM phosphate at pH 6.7 over the temperature range 283−303 K (Figure S1, Supporting Information). It is also worth noting that, compared with that in 20 mM phosphate at pH 6.7 throughout the temperature range examined, a small, but consistent increase in hydrodynamic radius was observed for mIL-3_{33-156} in 0.2 mM acetate at pH 4.3 (Table 1). This increase in hydrodynamic radius of mIL-3_{33-156} is in good agreement with the relatively poor spectral dispersion and broad line widths in acetate buffer, pH 4.3, and implies that a small degree of mIL-3_{33-156} aggregation in acetate buffer might contribute to the spectral deterioration observed when compared with the spectral dispersion and peak line width in phosphate buffer at pH 6.7. While the engineered version of mIL-3 (mIL-3_{33-156}) used in the present study exhibited significant improvement over the wild-type mIL-3 in terms of its solution behavior, and has enabled structural characterization of this cytokine to be performed, as discussed

Table 3. Average Values of ^{15}N R_1, R_2, and ^{15}N−{^{1}H} NOE of mIL-3_{33-156} for Relaxation Parameters Measured at both 283 and 298 K (ω_H = 600.13 MHz)

	T = 283 K			T = 298 K		
	R_1 (s^{-1})	R_2 (s^{-1})	NOE	R_1 (s^{-1})	R_2 (s^{-1})	NOE
overall[a]	1.39 ± 0.29	15.65 ± 5.59	0.57 ± 0.38	1.75 ± 0.31	11.33 ± 4.36	0.47 ± 0.51
helical regions[b]	1.33 ± 0.29	19.24 ± 2.94	0.79 ± 0.15	1.74 ± 0.29	13.54 ± 2.84	0.72 ± 0.10
helix A[c]	1.20 ± 0.21	20.02 ± 3.90	0.81 ± 0.13	1.58 ± 0.22	13.24 ± 2.55	0.74 ± 0.06
helix B[d]	1.46 ± 0.18	19.07 ± 2.83	0.82 ± 0.16	1.70 ± 0.20	12.99 ± 2.14	0.65 ± 0.12
helix C[e]	1.35 ± 0.34	18.68 ± 1.97	0.76 ± 0.19	2.03 ± 0.39	15.87 ± 3.98	0.72 ± 0.14
helix D[f]	1.35 ± 0.35	18.97 ± 2.67	0.79 ± 0.12	1.61 ± 0.16	12.35 ± 1.24	0.74 ± 0.08

[a] Averaged over 91 backbone amides. [b] Averaged over a total of 40 backbone amides within helical regions (α_A, Asn42−Leu54; α_B, Arg74−Glu87; α_C, Lys97−Cys106; and α_D, Leu124−His137). [c] Averaged over 12 residues within α_A (Asn42−Leu54). [d] Averaged over 8 residues within α_B (Arg74−Glu87). [e] Averaged over 9 residues within α_C (Lys97−Cys106). [f] Averaged over 11 residues within α_D (Leu124−His137).

dx.doi.org/10.1021/bi101810f |*Biochemistry* 2011, 50, 2464–2477

Table 4. Rotational Diffusion Parameters for mIL-$3_{33\text{-}156}$ Derived from ^{15}N Relaxation Data[a]

tensor	τ_m (10^{-9} s)[b]	D_{xx} (10^7 s^{-1})	D_{yy} (10^7 s^{-1})	D_{zz} (10^7 s^{-1})	$D_\parallel/D_\perp$ or D_{xx}:D_{yy}:D_{zz}	α (deg)	β/ϕ (deg)	γ/θ (deg)	χ^2	$\chi_{0.05}{}^2$[c]	F[d]
					***T* = 283 K (51 residues)**						
isotropic	11.05 (±0.11)								251	65	
axial (first min)	11.24[b]	1.30 (±0.13)	1.30 (±0.13)	1.85 (±0.25)	1.42		−45.3 (±13.0)	51.7 (±17.7)	236	61	1.00 (p = 0.505)
axial (second min)	10.75[b]	1.07 (±0.12)	1.79 (±0.13)	1.79 (±0.13)	0.60		16.4 (±8.3)	83.2 (±25.3)	221	61	2.13 (p = 0.005*)
anisotropic	10.77[b]	0.98 (±0.13)	1.72 (±0.15)	1.94 (±0.17)	0.51:0.89:1.00	−75.6 ± 8.2	−86.8 (±12.2)	−1.8 (±25.7)	220	59	m1: 1.64 (p = 0.049*), m2: 0.10 (p = 1.000)
					***T* = 283 K (26 residues)**						
isotropic	11.41 (±0.14)								143	36	
axial (first min)	11.82[b]	1.18 (±0.16)	1.18 (±0.16)	1.88 (±0.43)	1.59		68.0 (±17.2)	−10.3 (±7.6)	133	30	0.55 (p = 0.919)
axial (second min)[e]											
anisotropic	11.04[b]	0.85 (±0.24)	1.41 (±0.26)	2.27 (±0.53)	0.37:0.62:1.00	−82.6 (±25.3)	68.2 (±13.4)	−13.9 (±6.6)	131	28	m1: 0.15 (p = 1.000)
					***T* = 298 K (37 residues)**						
isotropic	7.65 (±0.05)								107	51	
axial (first min)	7.52[b]	2.04 (±0.05)	2.04 (±0.05)	2.57 (±0.12)	1.26		89.2 (±9.0)	−56.0 (±9.4)	88	46	2.38 (p = 0.006*)
axial (second min)	7.71[b]	1.89 (±0.07)	2.30 (±0.05)	2.30 (±0.05)	0.82		53.2 (±14.8)	35.1 (±12.5)	86	45	2.69 (p = 0.002*)
anisotropic	7.51[b]	1.82 (±0.30)	2.19 (±0.27)	2.64 (±0.69)	0.69:0.83:1.00	−84.0 (±23.7)	−85.8 (±16.0)	−42.7 (±19.4)	84	43	m1: 0.74 (p = 0.801), m2: 0.37 (p = 0.997)
					***T* = 298 K (26 residues)**						
isotropic	7.65 (±0.06)								78	38	
axial (first min)	7.82[b]	1.89 (±0.17)	1.89 (±0.17)	2.60 (±0.41)	1.38		83.5 (±13.6)	−30.9 (±12.2)	67	34	1.20 (p = 0.325)
axial (second min)											
anisotropic	7.34[b]	1.25 (±0.30)	2.15 (±0.29)	3.42 (±0.69)	0.37:0.63:1.00	−75.0 (±13.1)	80.9 (±11.8)	−29.4 (±9.7)	61	32	m1: 0.98 (p = 0.512)

[a] All rotational diffusion tensor parameters shown were obtained with the program TENSOR2[34] using the closest to mean solution structure of mIL-3_{33-156}. Uncertainties from the mean for all of the parameters are from standard deviations of 500 Monte Carlo simulations. [b] For axially symmetric and anisotropic models, $\tau_m = 1/[2(D_{xx} + D_{yy} + D_{zz})]$. [c] $\chi_{0.05}{}^2$ refers to the α = 0.05 confidence limit for the relevant fit derived from 500 Monte Carlo simulations. As adopted by the program TENSOR2, $\chi_{exp}{}^2 > \chi_{0.05}{}^2$ for all three diffusion models at both temperatures indicates none of the diffusion models converged, possibly due to the presence of poorly defined regions near the N- and C-termini and local conformational heterogeneity. [d] F-statistics were calculated using $F = [(\chi_m{}^2 - \chi_n{}^2)(N - n)]/[\chi_n{}^2(n - m)]$, where N is the total number of residues involved in the fitting and n and m are fitted parameters ($n > m$) with corresponding fitting errors, $\chi_n{}^2$ and $\chi_m{}^2$. p values corresponding to each F-statistic (calculated using GraphPad software, http://www.graphpad.com) are shown in parentheses with an asterisk indicating statistically significant improvement over the model compared. [e] A satisfactory model was not obtained for the oblate approximation with the given subset of residues (with (i) relaxation parameters available at both temperatures and (ii) satisfying both steady-state ^{15}N−{^{1}H} NOE ≥ 0.65 and $|T_1/\langle T_1\rangle - T_2/\langle T_2\rangle| \leq 1.5$ SD conditions,[35] mostly from the helical regions). It is worth noting that the diffusion anisotropy (D_{xx}:D_{yy}:D_{zz}) at 283 and 298 K is very similar when the same subset of backbone amides was used in the evaluation of rotational diffusion models.

dx.doi.org/10.1021/bi101810f |*Biochemistry* 2011, 50, 2464–2477

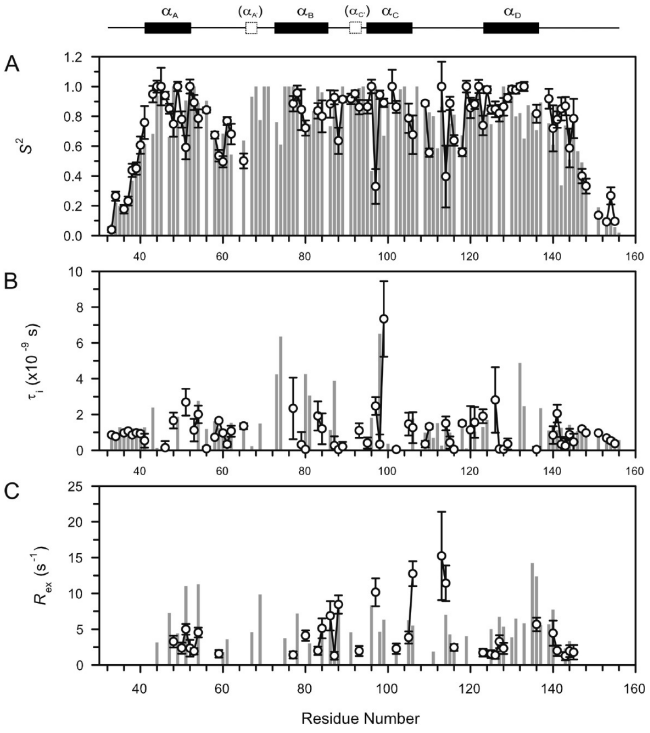

Figure 5. Model-free parameters for mIL-3_{33-156} obtained using backbone ^{15}N relaxation parameters as shown in Figure 4. An anisotropic rotational diffusion tensor model derived from a reduced group of 26 backbone amides was used (see Table 4). (A) The order parameter S^2 ($S_f^2 \times S_s^2$), (B) effective internal correlation time τ_i, and (C) apparent chemical shift and/or conformational exchange contribution R_{ex} to the translational relaxation R_2. A schematic showing secondary structural elements of mIL-3_{33-156} is shown at the top. Model-free parameters obtained with anisotropic rotational diffusion tensor parameter derived from the original group of residues (51 for 283 K and 37 for 298 K, respectively; see Table 4) are given in the Supporting Information (Table S3).

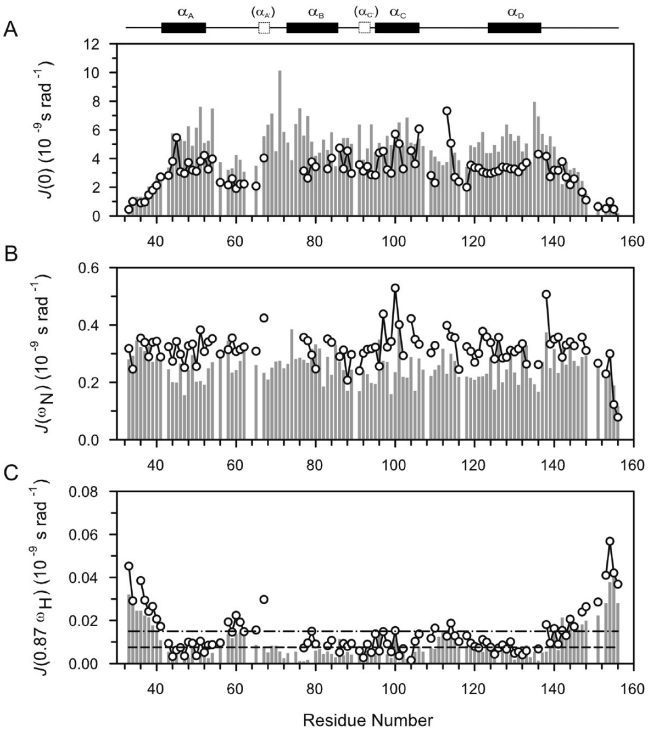

Figure 6. Reduced-spectral density functions of mIL-3_{33-156}. (A) $J(0)$, (B) $J(\omega_N)$, and (C) $J(0.87\omega_H)$ calculated from ^{15}N relaxation parameters measured at ^{15}N frequency of 60.81 MHz as shown in Figure 3 using eqs 2−5 at 283 K (gray bars) and 298 K (open circles). Dash and dot-dash-dot lines in (C) mark $J(0.87\omega_H)$ values at 7.5 and 15.0 ps rad^{-1}, respectively. A schematic showing secondary structural elements of mIL-3_{33-156} is shown at the top.

below, the intrinsic conformational heterogeneity within this molecule demonstrates that its solution properties are still quite complex. None of our data suggest that mIL-3_{33-156} undergoes aggregation over time, and thus we do not attribute any of these complex solution properties to aggregation; no changes were observed in either 1D ^{1}H or 2D ^{1}H−^{15}N HSQC spectra recorded several months apart at several temperatures between 283 and 303 K with storage at 4 °C during the intervening period (data not shown). Collectively, these data illustrate that mIL-3_{33-156} is not prone to aggregation at near neutral pH, consistent with its successful employment as a growth factor reagent in the laboratory.[11]

Backbone Dynamics on Picosecond to Nanosecond Time Scales. Model-free analysis is commonly used to extract residue-specific motional parameters on picosecond to nanosecond time scales from experimentally measured laboratory frame backbone ^{15}N relaxation parameters. In the present study, by using an anisotropic rotational diffusion model derived from a reduced group of residues with ^{15}N relaxation parameters satisfying both steady-state ^{15}N−{^{1}H} NOE ≥ 0.65 and $|T_1/\langle T_1\rangle - T_2/\langle T_2\rangle| \leq 1.5$ SD[35] at 283 and 298 K, most residues (103 out of 112 at 283 K and 86 out of 91 at 298 K) were fitted satisfactorily to one of five models. However, many residues display relatively longer internal correlation time (up to nanoseconds, models 2, 4, and 5), and a substantial number of residues required an R_{ex} term (model 3 and model 4) in order to be fitted satisfactorily. Clearly, the inaccuracy of the rotational diffusion tensor parameters used in the model-free analysis may have contributed to the overestimation of both internal correlation time, τ_i, and apparent chemical/conformational exchange contribution, R_{ex}. The elevated R_{ex} values are, however, consistent with the overall conformational heterogeneity of mIL-3 observed; reduced spectral density mapping where attempts to estimate approximate order parameters from $J(0)$ and $J(\omega_N)$[41,42] resulted in a large proportion of residues with S^2 values >1, strongly suggesting the presence of significant R_{ex} contributions to the experimentally measured R_2 values, as observed previously.[43] Contributions of conformational exchange to measured R_2 values have been reported previously to preclude conventional model-free analysis, such as in studies of cellular prion protein, PrP^c, which contains extended N- and C-termini[52] and the C-terminal domain of insulin-like growth factor binding protein 2.[53] With respect to the accuracy of the overall rotational diffusion tensor used in the model-free analysis of mIL-3_{33-156}, on one hand, the accuracy of rotational diffusion tensor may have been compromised by the presence of local conformational heterogeneity buried in the experimentally measured relaxation parameters. On the other hand, it may have also arisen from the incomplete representation of the distribution of orientations of N−H bond vectors by residues used in the determination of the rotational diffusion tensor, in particular for the diffusion tensor derived from the reduced group of residues where most of the residues are from the four α-helices (as shown previously),[54] even though the reduced

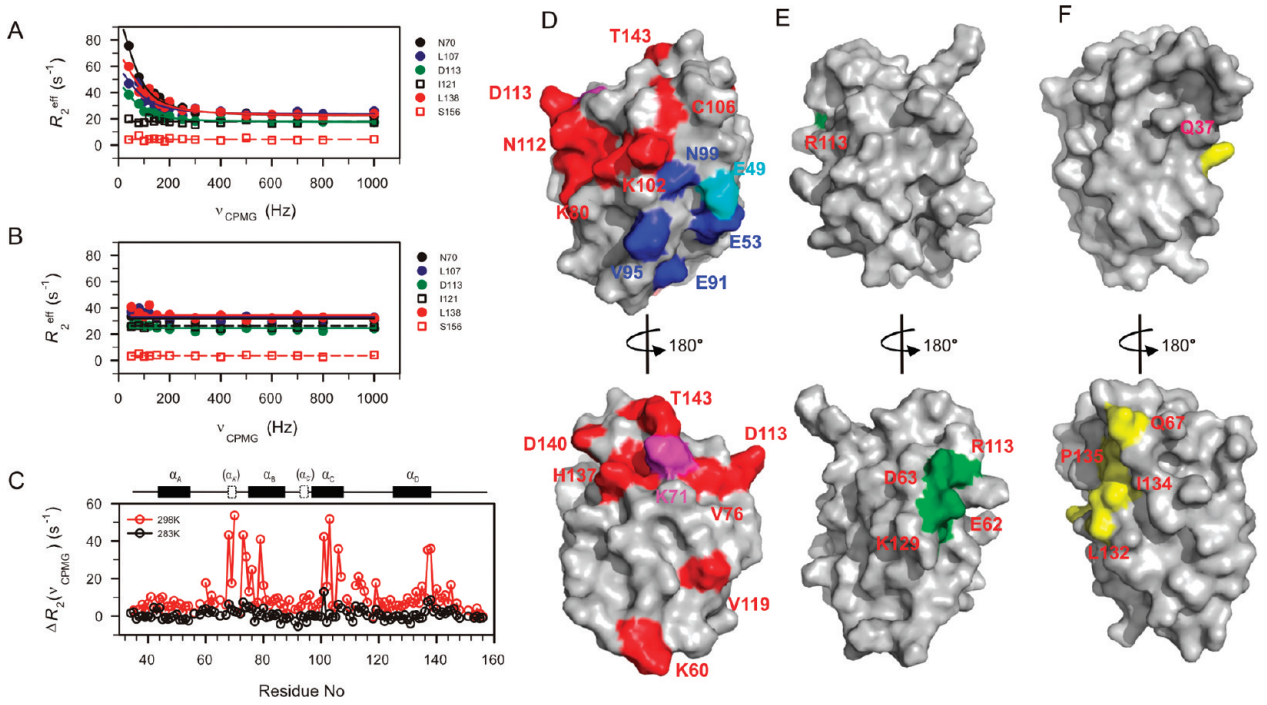

Figure 7. Summary of ^{15}N relaxation dispersion measurements for mIL-3_{33-156}. (A) ^{15}N relaxation dispersion curves for selected residues plotted as R_2^{eff} versus ν_{CPMG} at 298 K. (B) ^{15}N relaxation dispersion curves measured at 283 K for the same group of residues as in (A). Solid lines in (A) represent fit to eq 6 whereas dashed lines represent averaged values of $R_2^{eff}(\nu_{CPMG})$ for the given residues. In (B), both solid and dashed lines are averaged values of $R_2^{eff}(\nu_{CPMG})$. (C) The differences of effective transverse relaxation rates at different CPMG frequencies, $\Delta R_2^{eff}(\tau_{cp})$, are plotted against the residue number at 283 K ($\Delta R_2^{eff}(\nu_{CPMG}) = R_2^{eff}(50) - R_2^{eff}(1000)$) and 298 K ($\Delta R_2^{eff}(\nu_{CPMG}) = R_2^{eff}(40) - R_2^{eff}(1000)$), respectively. Also shown is a schematic of secondary structural elements of mIL-3_{33-156}. (D) Surface representation of mIL-3 with residues displaying ^{15}N relaxation dispersions at 298 K highlighted in red. Left-side view in the same orientation as Figure 2A (Lys71 and Ala111 are shown in magenta as their corresponding cross-peaks in the $^1H-^{15}N$ HSQC spectrum based ^{15}N relaxation dispersion measurements became too weak to measure). Residues important for β_{IL-3} receptor binding were highlighted in blue except for Glu43, which also displays relaxation dispersion at 298 K (shown in cyan). Surface representation of the human IL-3 analogue (PDB code 1JLI) (E) and human GM-CSF (PDB code 2GMF) (F) drawn in the same orientation as mIL-3 in panel D. Residues of human IL-3 important for α-receptor binding as defined by mutagenesis,[47] Glu62, Asp63, Arg113, and Lys129, are highlighted in green (E). Residues of human GM-CSF important for α-receptor interacting observed in the GM-CSF receptor complex crystal structure,[48] Val33, Gln37, Leu66, Gln67, Leu132, Val133, Ile134, and Pro135, are highlighted in yellow (F). The surface diagrams (D−F) were created using the program PyMOL (DeLano, 2004; http://pymol.sourceforge.net).

group of residues gave a better agreed anisotropy for the tensor model at two temperatures than the original groups (see Table 4).

From reduced spectral density functions, $J(0)$, $J(\omega_N)$, and $J(0.87\omega_H)$ (Figure 6), it is evident that mIL-3_{33-156} experiences more pronounced motions on millisecond to microsecond time scales at 283 K (Figure 6A) but has greater internal flexibility on the nanosecond time scale at 298 K (Figure 6B,C). This overall behavior is consistent with common characteristics of proteins in general as a function of temperature. As one would have anticipated, the N- and C-termini have greater flexibility with $J(0.87\omega_H) > 15$ ps rad^{-1}. Overall, α_A and α_D helices are more rigid than α_B and α_C helices, as the former have lower $J(0.87\omega_H)$ values (<7.5 ps rad^{-1}). On the other hand, the regions near residues (Glu49, Lys53, Glu91, Val95, and Asn99) within the α_A and α_C helices, recently shown by mutagenesis to play key roles in β_{IL-3} receptor recognition and activation,[17] are relatively rigid on picosecond to nanosecond time scales. These data are interesting, since they suggest that the intrinsic rigidity of this epitope may correspond with mIL-3's capacity to recognize its cognate β_{IL-3} receptor and facilitate direct binding with an affinity of ~14 nM.[55]

Local Conformational Heterogeneity. Elevated temperature often yields better spectra, as it decreases the overall tumbling time of a protein in solution and results in relatively sharp line widths, thereby improving spectral sensitivity and reducing spectral overlap. This is, however, not the case for mIL-3_{33-156}. Temperature coefficients of backbone amide protons that deviate from linearity and/or peaks of backbone amides that disappear at higher temperatures have been attributed to the presence of more than one conformation in certain regions of the protein undergoing fast and intermediate exchange, respectively.[40] Experimentally measured temperature coefficients of backbone amide chemical shifts have also been used to investigate low free-energy excited states of proteins[44] before ^{15}N relaxation dispersion measurements became the method of choice for exploring nuclear spins that have access to alternative conformations or low populated excited states.[56] In the present study, the majority of residues displaying nonlinear temperature dependence are clustered at one end of the α-helical bundle (Figure 3C). ^{15}N relaxation dispersion measurements provide direct experimental evidence for the presence of local low populated alternative states at 298 K. There is a strong correlation between residues displaying nonlinear temperature dependence and those exhibiting ν_{CPMG}-dependent R_2^{eff} in ^{15}N relaxation dispersion measurements (Figures 3C and 7C), indicating that residues clustering near one end of the α-helical bundle experience significant conformational exchange between the ground state and one or

more alternative states. As mentioned earlier, results from model-free analysis revealed a large number of residues undergoing substantial chemical/conformational exchange at both 283 and 298 K (see Figure 5C). The absence of transverse relaxation dispersion at 283 K (Figure 7B,C) would therefore imply that either the conformational exchange between ground state and alternative state, as observed at 298 K, has shifted all the way to one extreme or the interconversion has shifted to the slow exchange regime with a time constant outside that sensitive to the ^{15}N relaxation dispersion experiments. $^{1}H-^{15}N$ HSQC spectra were recorded at lower temperatures, including 278 K, but no additional peaks from possible minor structural species were detected (data not shown).

Conformational heterogeneity observed previously in NMR studies of the hIL-3 variant, SC-55494,[57] was attributed to *cis*−*trans* isomerization of four prolines within the α_A-α_B interhelix loop. As these four prolines are not conserved between hIL-3 variant SC-55494 and the mIL-3_{33-156} sequence (Figure S5B, Supporting Information), proline *cis*−*trans* isomerization cannot underlie the conformational heterogeneity observed in mIL-3_{33-156}. In fact, the regions within mIL-3_{33-156} that experience significant conformational heterogeneity correspond spatially to the sites within hIL-3, hIL-5, and hGM-CSF known to mediate the interaction with their respective α-receptor subunits (Figure 7D−F),[58] although the epitope on mIL-3 that mediates α-subunit binding has not yet been defined experimentally. This scenario parallels the conformational dynamics underlying the interaction of the growth factor, insulin-like growth factor (IGF)-II, with the C-terminal domain of insulin-like binding protein 6, where residues in the latter that access alternative conformations on a submillisecond to millisecond time scale (as detected through ^{15}N transverse relaxation dispersion measurements) correlated broadly with residues important for its binding to IGF-II.[30]

Recently, two overlapping epitopes on mIL-3 were shown to be critical for recognition and activation of the mIL-3-specific β-receptor (β_{IL-3}) in the presence of two distinct, naturally occurring splice isoforms of the mIL-3α subunit.[17] In contrast to the conformational heterogeneity evident for residues within the putative mIL-3Rα-interacting epitope (Figure 7D), the key β-receptor interacting residues located within the α_A helix (Glu49 and Lys53), the α_B-α_C loop (Glu91), and N-terminal portion of the α_C helix (Val95 and Asn99)[17] are relatively rigid on both picosecond to nanosecond and submillisecond to millisecond time scales except for Glu49, which exhibits motion on the time scale of submillisecond to millisecond at 298 K as identified from ^{15}N relaxation dispersion measurements. This raises the interesting possibility that the conformational flexibility of residues in the putative mIL-3Rα-interacting epitope might enable mIL-3 to sample different conformer populations, a property that may underlie its capacity to engage either of the two mIL-3Rα isoforms[9,17] and direct mIL-3 binding to distinct epitopes on the β_{IL-3} receptor to assemble structurally distinct signaling complexes,[17] capable of eliciting different signaling outputs.[9]

■ ASSOCIATED CONTENT

Supporting Information. $^{1}H-^{15}N$ HSQC spectra under various solution conditions (Figures S1 and S2), a summary of backbone angular order parameters of the mIL-3_{33-156} ensemble (Figure S3), representative R_1 and R_2 decay curves including nonlinear regression for a group of selected residues (Figure S4), ribbon diagrams and sequence alignments of mIL-3, hIL-3, GM-CSF, and hIL-5 (Figure S5), and tables summarizing experimentally measured ^{15}N relaxation parameters (Table S1), motional parameters resulting from model-free analysis (Tables S2, S3, and S4), and fitting outcomes of ^{15}N relaxation dispersion data (Tables S5). This material is available free of charge via the Internet at http://pubs.acs.org.

Accession Codes

Coordinates for the final set of 20 structures of mIL-3_{33-156} and associated structural restraints have been deposited in the Protein Data Bank with accession number 2L3O.

■ AUTHOR INFORMATION

Corresponding Author

*S.Y.: tel, 61 3 93452332; fax, 61 3 93470852; e-mail, syao@wehi.edu.au. J.M.M.: tel, 61 3 93452407; fax, 61 3 93470852; e-mail, jamesm@wehi.edu.au.

Funding Sources

This work was supported in part by the National Health and Medical Research Council (NHMRC), Australia (Program Grant 461219), IRIISS Grant 361646, and a Victorian State Government OIS grant. Fellowship support was provided by the NHMRC (R.S.N., J.M.M.) and the Australian Research Council (Grant FT100100100 to J.M.M.).

■ ACKNOWLEDGMENT

The authors acknowledge the access to the NMR facility at Bio21 Institute, The University of Melbourne.

■ ABBREVIATIONS

GM-CSF, granulocyte-macrophage colony-stimulating factor; IL-3, interleukin-3; IL-5, interleukin-5; mIL-3, murine interleukin-3; mIL-3_{33-156}, residues 33−156 of mIL-3 with the substitution of an alanine for Cys105; β_{IL-3}, mIL-3 specific β-receptor subunit; NMR, nuclear magnetic resonance; PFG-NMR, pulsed-field-gradient NMR; rms, root mean square.

■ REFERENCES

(1) Hapel, A. J., Fung, M. C., Johnson, R. M., Young, I. G., Johnson, G., and Metcalf, D. (1985) Biologic properties of molecularly cloned and expressed murine interleukin-3. *Blood 65*, 1453–1459.

(2) Robin, C., Ottersbach, K., Durand, C., Peeters, M., Vanes, L., Tybulewicz, V., and Dzierzak, E. (2006) An unexpected role for IL-3 in the embryonic development of hematopoietic stem cells. *Dev. Cell 11*, 171–180.

(3) Lantz, C. S., Boesiger, J., Song, C. H., Mach, N., Kobayashi, T., Mulligan, R. C., Nawa, Y., Dranoff, G., and Galli, S. J. (1998) Role for interleukin-3 in mast-cell and basophil development and in immunity to parasites. *Nature 392*, 90–93.

(4) Perrigoue, J. G., Saenz, S. A., Siracusa, M. C., Allenspach, E. J., Taylor, B. C., Giacomin, P. R., Nair, M. G., Du, Y., Zaph, C., van Rooijen, N., Comeau, M. R., Pearce, E. J., Laufer, T. M., and Artis, D. (2009) MHC class II-dependent basophil-CD4+ T cell interactions promote T(H)2 cytokine-dependent immunity. *Nat. Immunol. 10*, 697–705.

(5) Sokol, C. L., Chu, N. Q., Yu, S., Nish, S. A., Laufer, T. M., and Medzhitov, R. (2009) Basophils function as antigen-presenting cells for an allergen-induced T helper type 2 response. *Nat. Immunol. 10*, 713–720.

(6) Itoh, N., Yonehara, S., Schreurs, J., Gorman, D. M., Maruyama, K., Ishii, A., Yahara, I., Arai, K., and Miyajima, A. (1990) Cloning of an interleukin-3 receptor gene: a member of a distinct receptor gene family. *Science 247*, 324–327.

(7) Quelle, F. W., Sato, N., Witthuhn, B. A., Inhorn, R. C., Eder, M., Miyajima, A., Griffin, J. D., and Ihle, J. N. (1994) JAK2 associates with the βc chain of the receptor for granulocyte-macrophage colony-stimulating factor, and its activation requires the membrane-proximal region. *Mol. Cell. Biol. 14*, 4335–4341.

(8) Sakamaki, K., Miyajima, I., Kitamura, T., and Miyajima, A. (1992) Critical cytoplasmic domains of the common β subunit of the human GM-CSF, IL-3 and IL-5 receptors for growth signal transduction and tyrosine phosphorylation. *EMBO J. 11*, 3541–3549.

(9) Chen, J., Olsen, J., Ford, S., Mirza, S., Walker, A., Murphy, J. M., and Young, I. G. (2009) A new isoform of interleukin-3 receptor α with novel differentiation activity and high affinity binding mode. *J. Biol. Chem. 284*, 5763–5773.

(10) Clark-Lewis, I., Hood, L. E., and Kent, S. B. (1988) Role of disulfide bridges in determining the biological activity of interleukin 3. *Proc. Natl. Acad. Sci. U.S.A. 85*, 7897–7901.

(11) Murphy, J. M., Metcalf, D., Young, I. G., and Hilton, D. J. (2010) A convenient method for preparation of an engineered mouse interleukin-3 analog with high solubility and wild-type bioactivity. *Growth Factors 28*, 104–110.

(12) Feng, Y., Klein, B. K., Vu, L., Aykent, S., and McWherter, C. A. (1995) ^{1}H, ^{13}C, and ^{15}N NMR resonance assignments, secondary structure, and backbone topology of a variant of human interleukin-3. *Biochemistry 34*, 6540–6551.

(13) Feng, Y., Klein, B. K., and McWherter, C. A. (1996) Three-dimensional solution structure and backbone dynamics of a variant of human interleukin-3. *J. Mol. Biol. 259*, 524–541.

(14) Ihle, J. N., Keller, J., Oroszlan, S., Henderson, L. E., Copeland, T. D., Fitch, F., Prystowsky, M. B., Goldwasser, E., Schrader, J. W., Palaszynski, E., Dy, M., and Lebel, B. (1983) Biologic properties of homogeneous interleukin 3. I. Demonstration of WEHI-3 growth factor activity, mast cell growth factor activity, p cell-stimulating factor activity, colony-stimulating factor activity, and histamine-producing cell-stimulating factor activity. *J. Immunol. 131*, 282–287.

(15) Milburn, M. V., Hassell, A. M., Lambert, M. H., Jordan, S. R., Proudfoot, A. E., Graber, P., and Wells, T. N. (1993) A novel dimer configuration revealed by the crystal structure at 2.4 Å resolution of human interleukin-5. *Nature 363*, 172–176.

(16) Walter, M. R., Cook, W. J., Ealick, S. E., Nagabhushan, T. L., Trotta, P. P., and Bugg, C. E. (1992) Three-dimensional structure of recombinant human granulocyte-macrophage colony-stimulating factor. *J. Mol. Biol. 224*, 1075–1085.

(17) Mirza, S., Chen, J., Wen, B., Ewens, C. L., Dai, J., Murphy, J. M., and Young, I. G. (2010) Two modes of β-receptor recognition are mediated by distinct epitopes on mouse and human interleukin-3. *J. Biol. Chem. 285*, 22370–22381.

(18) Yao, S., Murphy, J. M., Low, A., and Norton, R. S. (2010) ^{1}H, ^{13}C and ^{15}N resonance assignments of a highly-soluble murine interleukin-3 analogue with wild-type bioactivity. *Biomol. NMR Assign. 4*, 73–77.

(19) Wilkins, D. K., Grimshaw, S. B., Receveur, V., Dobson, C. M., Jones, J. A., and Smith, L. J. (1999) Hydrodynamic radii of native and denatured proteins measured by pulse field gradient NMR techniques. *Biochemistry 38*, 16424–16431.

(20) Yao, S., Howlett, G. J., and Norton, R. S. (2000) Peptide self-association in aqueous trifluoroethanol monitored by pulsed field gradient NMR diffusion measurements. *J. Biomol. NMR 16*, 109–119.

(21) Yao, S., Babon, J. J., and Norton, R. S. (2008) Protein effective rotational correlation times from translational self-diffusion coefficients measured by PFG-NMR. *Biophys. Chem. 136*, 145–151.

(22) Cornilescu, G., Delaglio, F., and Bax, A. (1999) Protein backbone angle restraints from searching a database for chemical shift and sequence homology. *J. Biomol. NMR 13*, 289–302.

(23) Ludvigsen, S., and Poulsen, F. M. (1992) Positive Phi-angles in proteins by nuclear magnetic resonance spectroscopy. *J. Biomol. NMR 2*, 227–233.

(24) Herrmann, T., Guntert, P., and Wüthrich, K. (2002) Protein NMR structure determination with automated NOE assignment using the new software CANDID and the torsion angle dynamics algorithm DYANA. *J. Mol. Biol. 319*, 209–227.

(25) Schwieters, C. D., Kuszewski, J. J., Tjandra, N., and Clore, G. M. (2003) The Xplor-NIH NMR molecular structure determination package. *J. Magn. Reson. 160*, 65–73.

(26) Linge, J. P., Williams, M. A., Spronk, C. A., Bonvin, A. M., and Nilges, M. (2003) Refinement of protein structures in explicit solvent. *Proteins 50*, 496–506.

(27) Laskowski, R. A., Rullmannn, J. A., MacArthur, M. W., Kaptein, R., and Thornton, J. M. (1996) AQUA and PROCHECK-NMR: programs for checking the quality of protein structures solved by NMR. *J. Biomol. NMR 8*, 477–486.

(28) Koradi, R., Billeter, M., and Wüthrich, K. (1996) MOLMOL: a program for display and analysis of macromolecular structures. *J. Mol. Graphics 14* (51−55), 29–32.

(29) Berman, H. M., Battistuz, T., Bhat, T. N., Bluhm, W. F., Bourne, P. E., Burkhardt, K., Feng, Z., Gilliland, G. L., Iype, L., Jain, S., Fagan, P., Marvin, J., Padilla, D., Ravichandran, V., Schneider, B., Thanki, N., Weissig, H., Westbrook, J. D., and Zardecki, C. (2002) The Protein Data Bank. *Acta Crystallogr., Sect. D: Biol. Crystallogr. 58*, 899–907.

(30) Yao, S., Headey, S. J., Keizer, D. W., Bach, L. A., and Norton, R. S. (2004) C-terminal domain of insulin-like growth factor (IGF) binding protein 6: conformational exchange and its correlation with IGF-II binding. *Biochemistry 43*, 11187–11195.

(31) Yao, S., Liu, M. S., Masters, S. L., Zhang, J. G., Babon, J. J., Nicola, N. A., Nicholson, S. E., and Norton, R. S. (2006) Dynamics of the SPRY domain-containing SOCS box protein 2: flexibility of key functional loops. *Protein Sci. 15*, 2761–2772.

(32) Bartels, C., Xia, T. H., Billeter, M., Güntert, P., and Wüthrich, K. (1995) The program XEASY for computer-supported NMR spectral-analysis of biological macromolecules. *J. Biomol. NMR 6*, 1–10.

(33) Farrow, N. A., Muhandiram, R., Singer, A. U., Pascal, S. M., Kay, C. M., Gish, G., Shoelson, S. E., Pawson, T., Forman-Kay, J. D., and Kay, L. E. (1994) Backbone dynamics of a free and a phosphopeptide-complexed Src homology-2 domain studied by ^{15}N NMR relaxation. *Biochemistry 33*, 5984–6003.

(34) Dosset, P., Hus, J. C., Blackledge, M., and Marion, D. (2000) Efficient analysis of macromolecular rotational diffusion from heteronuclear relaxation data. *J. Biomol. NMR 16*, 23–28.

(35) Tjandra, N., Kuboniwa, H., Ren, H., and Bax, A. (1995) Rotational dynamics of calcium-free calmodulin studied by ^{15}N-NMR relaxation measurements. *Eur. J. Biochem. 230*, 1014–1024.

(36) Farrow, N. A., Zhang, O., Szabo, A., Torchia, D. A., and Kay, L. E. (1995) Spectral density function mapping using ^{15}N relaxation data exclusively. *J. Biomol. NMR 6*, 153–162.

(37) Loria, J. P., Rance, M., and Palmer, A. G. (1999) A relaxation-compensated Carr-Purcell-Meiboom-Gill sequence for characterizing chemical exchange by NMR spectroscopy. *J. Am. Chem. Soc. 121*, 2331–2332.

(38) Mulder, F. A., Skrynnikov, N. R., Hon, B., Dahlquist, F. W., and Kay, L. E. (2001) Measurement of slow (μs-ms) time scale dynamics in protein side chains by ^{15}N relaxation dispersion NMR spectroscopy: application to Asn and Gln residues in a cavity mutant of T4 lysozyme. *J. Am. Chem. Soc. 123*, 967–975.

(39) Lux, Z., and Meiboom, S. (1963) Nuclear magnetic resonance study of the protolysis of trimethylammonium ion in aqueous solution —order of the reaction with respect to solvent. *J. Chem. Phys.* 366–370.

(40) Baxter, N. J., and Williamson, M. P. (1997) Temperature dependence of ^{1}H chemical shifts in proteins. *J. Biomol. NMR 9*, 359–369.

(41) Lefevre, J. F., Dayie, K. T., Peng, J. W., and Wagner, G. (1996) Internal mobility in the partially folded DNA binding and dimerization domains of GAL4: NMR analysis of the N-H spectral density functions. *Biochemistry 35*, 2674–2686.

(42) Bracken, C., Carr, P. A., Cavanagh, J., and Palmer, A. G., III (1999) Temperature dependence of intramolecular dynamics of the basic leucine zipper of GCN4: implications for the entropy of association with DNA. *J. Mol. Biol. 285*, 2133–2146.

(43) O'Sullivan, D. B., Jones, C. E., Abdelraheim, S. R., Brazier, M. W., Toms, H., Brown, D. R., and Viles, J. H. (2009) Dynamics of a truncated prion protein, PrP(113−231), from ^{15}N NMR relaxation: order parameters calculated and slow conformational fluctuations localized to a distinct region. *Protein Sci. 18*, 410–423.

(44) Baxter, N. J., Hosszu, L. L., Waltho, J. P., and Williamson, M. P. (1998) Characterisation of low free-energy excited states of folded proteins. *J. Mol. Biol. 284*, 1625–1639.

(45) Eisenmesser, E. Z., Bosco, D. A., Akke, M., and Kern, D. (2002) Enzyme dynamics during catalysis. *Science 295*, 1520–1523.

(46) Boehr, D. D., McElheny, D., Dyson, H. J., and Wright, P. E. (2006) The dynamic energy landscape of dihydrofolate reductase catalysis. *Science 313*, 1638–1642.

(47) Olins, P. O., Bauer, S. C., Braford-Goldberg, S., Sterbenz, K., Polazzi, J. O., Caparon, M. H., Klein, B. K., Easton, A. M., Paik, K., Klover, J. A., Thiele, B. R., and McKearn, J. P. (1995) Saturation mutagenesis of human interleukin-3. *J. Biol. Chem. 270*, 23754–23760.

(48) Hansen, G., Hercus, T. R., McClure, B. J., Stomski, F. C., Dottore, M., Powell, J., Ramshaw, H., Woodcock, J. M., Xu, Y., Guthridge, M., McKinstry, W. J., Lopez, A. F., and Parker, M. W. (2008) The structure of the GM-CSF receptor complex reveals a distinct mode of cytokine receptor activation. *Cell 134*, 496–507.

(49) Mirza, S., Walker, A., Chen, J., Murphy, J. M., and Young, I. G. (2010) The Ig-like domain of human GM-CSF receptor α plays a critical role in cytokine binding and receptor activation. *Biochem. J. 426*, 307–317.

(50) Abdel-Meguid, S. S., Shieh, H. S., Smith, W. W., Dayringer, H. E., Violand, B. N., and Bentle, L. A. (1987) Three-dimensional structure of a genetically engineered variant of porcine growth hormone. *Proc. Natl. Acad. Sci. U.S.A. 84*, 6434–6437.

(51) Dickason, R. R., and Huston, D. P. (1996) Creation of a biologically active interleukin-5 monomer. *Nature 379*, 652–655.

(52) Viles, J. H., Donne, D., Kroon, G., Prusiner, S. B., Cohen, F. E., Dyson, H. J., and Wright, P. E. (2001) Local structural plasticity of the prion protein. Analysis of NMR relaxation dynamics. *Biochemistry 40*, 2743–2753.

(53) Kuang, Z., Yao, S., Keizer, D. W., Wang, C. C., Bach, L. A., Forbes, B. E., Wallace, J. C., and Norton, R. S. (2006) Structure, dynamics and heparin binding of the C-terminal domain of insulin-like growth factor-binding protein-2 (IGFBP-2). *J. Mol. Biol. 364*, 690–704.

(54) Lee, L. K., Rance, M., Chazin, W. J., and Palmer, A. G., III (1997) Rotational diffusion anisotropy of proteins from simultaneous analysis of ^{15}N and $^{13}C^{\alpha}$ nuclear spin relaxation. *J. Biomol. NMR 9*, 287–298.

(55) Mirza, S., Chen, J., Murphy, J. M., and Young, I. G. (2010) The role of interchain heterodisulfide formation in activation of the human common β and mouse $\beta_{IL\text{-}3}$ receptors. *J. Biol. Chem. 285*, 24759–24768.

(56) Mittermaier, A. K., and Kay, L. E. (2009) Observing biological dynamics at atomic resolution using NMR. *Trends Biochem. Sci. 34*, 601–611.

(57) Feng, Y., Hood, W. F., Forgey, R. W., Abegg, A. L., Caparon, M. H., Thiele, B. R., Leimgruber, R. M., and McWherter, C. A. (1997) Multiple conformations of a human interleukin-3 variant. *Protein Sci. 6*, 1777–1782.

(58) Murphy, J. M., and Young, I. G. (2006) IL-3, IL-5, and GM-CSF signaling: crystal structure of the human β-common receptor. *Vitam. Horm. 74*, 1–30.